



Hydrogen Peroxide Versus Hydrogen Generation at Bipolar Pd/Au Nano-catalysts Grown into an Intrinsically Microporous Polyamine (PIM-EA-TB)

Lina Wang¹ · Mariolino Carta² · Richard Malpass-Evans³ · Neil B. McKeown³ · Philip J. Fletcher⁴ · Diana Lednitzky⁴ · Frank Marken¹

Accepted: 25 September 2021 / Published online: 9 October 2021
© The Author(s) 2021

Abstract

Binding of PdCl₄²⁻ into the polymer of intrinsic microporosity PIM-EA-TB (on a Nylon mesh substrate) followed by borohydride reduction leads to uncapped Pd(0) nano-catalysts with typically 3.2 ± 0.2 nm diameter embedded within the microporous polymer host structure. Spontaneous reaction of Pd(0) with formic acid and oxygen is shown to result in the competing formation of (i) hydrogen peroxide (at low formic acid concentration in air; with optimum H₂O₂ yield at 2 mM HCOOH), (ii) water, or (iii) hydrogen (at higher formic acid concentration or under argon). Next, a spontaneous electroless gold deposition process is employed to attach gold (typically 10- to 35-nm diameter) to the nano-palladium in PIM-EA-TB to give an order of magnitude enhanced production of H₂O₂ with high yields even at higher HCOOH concentration (suppressing hydrogen evolution). Pd and Au work hand-in-hand as bipolar electrocatalysts. A Clark probe method is developed to assess the catalyst efficiency (based on competing oxygen removal and hydrogen production) and a mass spectrometry method is developed to monitor/optimize the rate of production of hydrogen peroxide. Heterogenised Pd/Au@PIM-EA-TB catalysts are effective and allow easy catalyst recovery and reuse for hydrogen peroxide production.

Keywords Biomass · Disinfection · Heterogenised palladium · Epoxidation · Hydrogen

Introduction

Microporous environments are commonly employed for immobilisation of catalysts (i) to control/restrict reagent access, (ii) to enhance the accessible catalyst surface area, (iii) to recover and re-use catalysts, and (iv) to improve the catalyst micro-environment and catalyst efficiency for example for palladium catalysts [1]. Palladium has found

a plethora of applications in catalysis in processes ranging from C–C coupling chemistry [2] and N-alkylation, [3] in H₂O₂ production [4, 5] (see also Pd–Au catalysis for “green” H₂O₂ production [6] and for the selective oxidation of methane [7], alcohol oxidation [8], in hydrogen generation from formic acid,[9] in electrocatalysis [10], and in a wide range of catalytic reduction reactions [11]. Immobilisation of Pd nanoparticles into microporous hosts is linked to enhanced catalytic reactivity as long as (i) host–guest interactions do not cause blocking and (ii) permeation of reactants into the host is effective. There is one previous report on the immobilisation of Pd nanoparticle catalysts into the polymer of intrinsic microporosity (abbreviated PIM) PIM-1 [12]. Fibrous PIM-1 with Pd nanoparticles embedded were obtained by electrospinning and employed in the catalytic reduction of nitroaromatics. It was shown that the PIM-1 provided selectivity towards the more strongly absorbing reactants and good permeation. Palladium inside of the microporous PIM-1 was demonstrated to be catalytically active. Palladium catalysts have been immobilised in other types of microporous hosts such as metal–organic

✉ Frank Marken
f.marken@bath.ac.uk

¹ Department of Chemistry, University of Bath, Claverton Down, Bath BA2 7AY, UK

² Department of Chemistry, College of Science, Swansea University, Grove Building, Singleton Park, SA2 8PP Swansea, UK

³ School of Chemistry, University of Edinburgh, Joseph Black Building, West Mains Road, Edinburgh EH9 3JJ, Scotland, UK

⁴ Materials & Chemical Characterisation Facility, University of Bath, Bath BA2 7AY, MC, UK

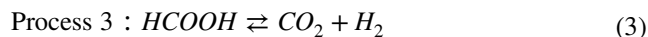
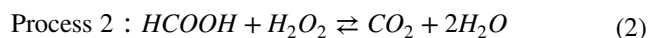
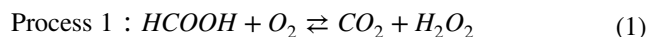
frameworks [13]. Here, palladium is immobilised into the polymer of intrinsic microporosity PIM-EA-TB (see molecular structure in Fig. 1).

The development of polymers of intrinsic microporosity (PIMs) was linked initially to the formation of gas permeable and gas-separation membrane materials [14, 15]. Only recently have wet-chemical applications for intrinsically microporous polymers emerged, for example, in electrochemistry [16, 17], in electrocatalysis with embedded molecular catalysts [18] or embedded nanoparticle catalysts for hydrogen production [19, 20], and for hydrogen peroxide [21] production. PIM-EA-TB offers a microporous host material with typically $1000 \text{ m}^2 \text{ g}^{-1}$ surface area (based on Brunauer–Emmett–Teller nitrogen adsorption data [22]) and with rigid microchannels of typically 1–2 nm diameter. Films of PIM-EA-TB on electrodes or sensors are produced by cast deposition from solvent [23].

Hydrogen peroxide formation is important in disinfection [24], in biomass break-down [25, 26], in pollution treatment [27], and in many further areas of chemical technologies [28]. Hydrogen peroxide can be generated conveniently from ambient oxygen, but the efficiency for this process is often problematic primarily due to unwanted over-reduction or disproportionation of H_2O_2 into $\text{H}_2\text{O}/\text{O}_2$. New types of sustainable single-atom catalysts for the conversion of oxygen into hydrogen peroxide are under development [29]. Although photolytic processes are successfully employed to drive the reduction of O_2 to H_2O_2 [30], there are also some successful dark chemical processes based on ambient oxygen and chemical reducing agents such as glucose [31] or formic acid [32].

In this report, the immobilisation/heterogenisation of a Pd catalyst or a Pd/Au catalyst into the micropores of the molecularly rigid PIM-EA-TB polyamine is investigated. It is shown that Pd nanoparticles of typically 3.2-nm diameter are readily synthesised by absorption of PdCl_4^{2-} followed by borohydride reduction. These “guest” nanoparticles are active for hydrogen generation from formic acid due to PIM-EA-TB not blocking the surface of the catalyst and effective permeation of formic acid. Both hydrogen production

and oxygen consumption are monitored in situ with a Clark probe [33] (Fig. 1A) and employing Nylon mesh substrates. Processes at the palladium catalyst are tentatively suggested to be based on (A) oxygen consumption (see processes 1 and 2) and based on (B) hydrogen production (process 3).



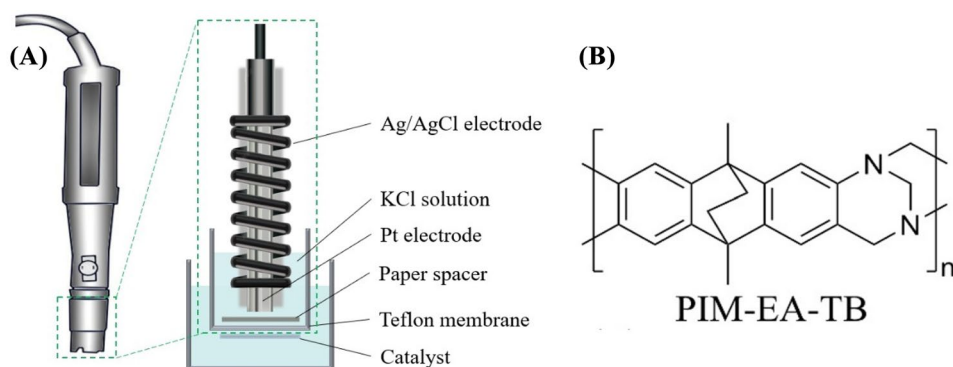
Spontaneous gold growth onto the palladium nanoparticles as nucleation sites is employed to moderate catalyst activity for hydrogen generation and to enhance the rate of hydrogen peroxide production by an order of magnitude. The competing mechanisms, the bipolar nature of the Pd/Au catalyst, and the role of the polymer of intrinsic microscopy are discussed.

Experimental

Reagents

HCl (ACS reagent, 37%), PdCl_2 (99%), NaBH_4 (powder, 98%), KAuCl_4 (98%), H_3PO_4 (85 wt.% solution, ACS Reagent), HCOOH (96%, ACS Reagent), Na_2CO_3 (powder, $\geq 99.5\%$, ACS Reagent), and p-nitrophenylboronic acid ($\geq 95.0\%$) were purchased from Sigma–Aldrich. H_2O_2 (ACS Reagent, 30 wt.% in H_2O) and dimethyl sulfoxide (DMSO, for HPLC, $\geq 99.7\%$) were products from Honeywell. NaHCO_3 ($\geq 99.7\%$) and NaOH (pellets, laboratory reagent grade) were obtained from Fluka. Jovitec universal pH test paper (pH full range 1–14) was applied to monitor the pH value of solutions in the H_2O_2 quantification experiments. PIM-EA-TB was synthesised following the literature recipe [34]. Nylon mesh from 75- μm diameter Nylon was purchased from Amazon.com (therpin reusable Nylon fine mesh food strainer bag).

Fig. 1 **A** Schematic drawing of a Clark probe for in situ analysis of oxygen consumption and hydrogen production. **B** Molecular structure of PIM-EA-TB



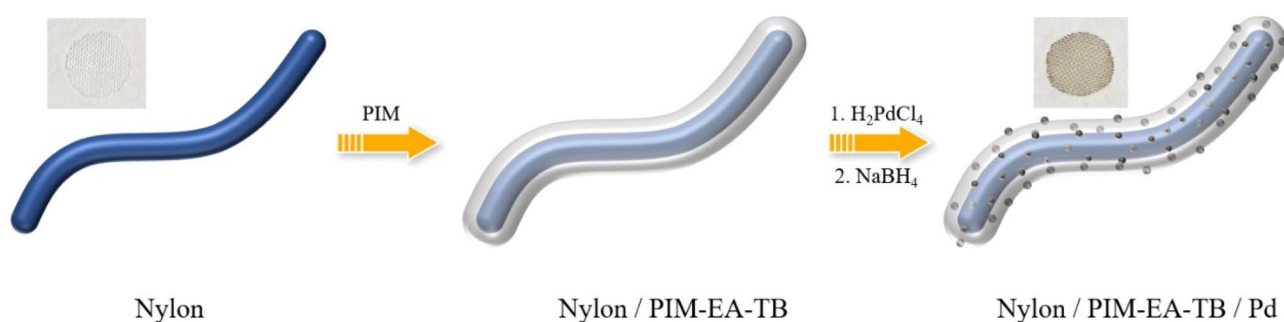


Fig. 2 Illustration of the use of a Nylon substrate that is coated with PIM-EA-TB and then exposed to PdCl_4^{2-} followed by rinsing, drying, and reduction in borohydride reduction to give Pd nanoparticles embedded in the PIM-EA-TB host

Instrumentation

Clark-type polarographic dissolved oxygen probe (HI76407) and corresponding electrolyte fill solution (HI7041S) were the products of Hanna Instruments Ltd. A thin tissue layer (Whatman Schleicher & Schuell 105 lens cleaning tissue) was introduced to maintain the distance from platinum electrode to the Teflon membrane. Ultra-pure water (resistivity not less than $18.2 \text{ M}\Omega \text{ cm}$ at 20°C) was taken from Thermo Scientific water purification equipment. A pH meter (Jenway 3505) was used to monitor the pH of buffer solutions. The morphology of the Pd@PIM-EA-TB and Pd/Au@PIM-EA-TB nanoparticles were evaluated using a scanning electron microscope (SEM, Hitachi SU3900) and a transmission electron microscope (TEM, JEOL JEM-2100PLUS). Elemental mapping was carried out with an attached energy dispersive X-ray analyser (170 mm^2 Ultim Max EDX). Electrochemical experiments were performed with a computer-controlled potentiostat (Metrohm microAutolab II). The quantification of H_2O_2 was carried out by liquid chromatography-mass spectroscopy (LC-MS) technique with an Agilent 6545 Accurate-Mass Q-TOF LC/MS system.

Procedures

Formation of Pd@PIM-EA-TB

A Nylon substrate was employed to investigate the catalytic activity of heterogenised catalysts. A disk of 8-mm diameter with Nylon strands of $75\text{-}\mu\text{m}$ diameter was first coated with PIM-EA-TB (approx. $20 \mu\text{g}$). Next, the modified Nylon disk was immersed into 5 mM PdCl_4^{2-} in 1 M HCl . Under these conditions, the PIM-EA-TB is protonated and PdCl_4^{2-} is accumulated into the microporous polymer which is visible as yellow coloration [35]. Next, the disks are immersed into 0.13 M NaBH_4 solution in water and left to react in the dark in a refrigerator (4°C , 20 h , see Fig. 2).

Figure 3 shows scanning electron microscopy (SEM) images for the distribution of deposits on the Nylon mesh. White regions in Fig. 3A are consistent with regions of more Pd metal deposits accumulated due to a higher PIM-EA-TB loading. An enhanced presence of Pd at Nylon thread intersections is due to a higher amount of PIM-EA-TB in these regions caused capillary forces during evaporation of the deposition solution. Pd appears to be distributed in the form of uniformly sized nanoparticles (vide infra) within the PIM-EA-TB.

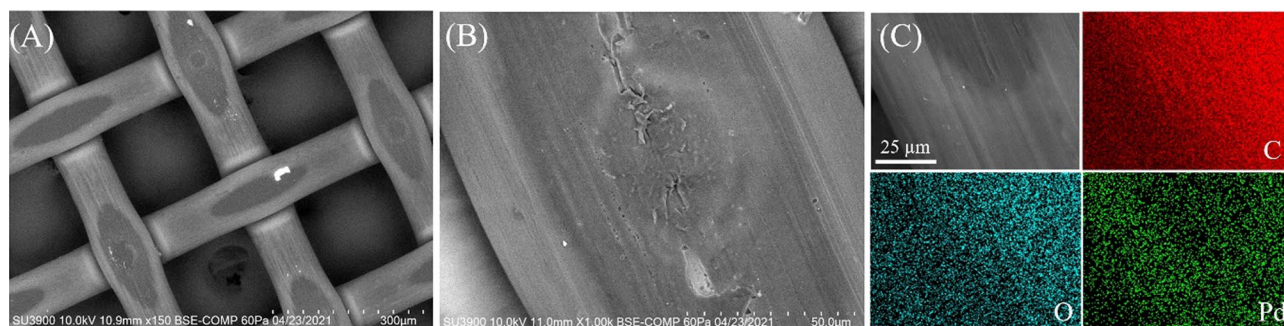


Fig. 3 Scanning electron microscopy (SEM) images **A**, **B** and energy-dispersive X-ray spectroscopy (EDX) elemental mapping analysis **C** for Pd@PIM-EA-TB coated Nylon mesh

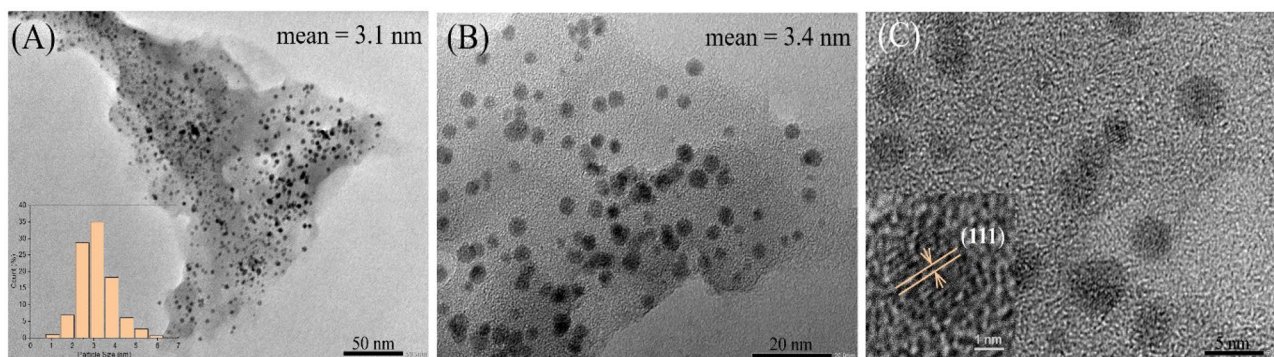


Fig. 4 Transmission electron microscopy (TEM) images for Pd@PIM-EA-TB. **A** Pd nanoparticles with mean size of 3.2 ± 0.2 nm evenly distributed in PIM-EA-TB (inset: size distribution of Pd nano-

particles). **B** Higher magnification image with mean Pd particle size of 3.4 nm. **C** High-resolution image showing the (111) crystal facet of Pd

In order to better image Pd nanoparticles, samples were ultrasonicated in isopropanol, and then solution phase was deposited onto transmission electron microscopy (TEM) grids. Figure 4 shows typical images for PIM-EA-TB with nanoparticles embedded. Particle size analysis suggests typically 3.2 ± 2.0 nm diameter.

Formation of Nano-Pd/Au@PIM-EA-TB

The spontaneous formation of gold deposits on palladium is driven by the high Au(0/III) standard potential driving oxygen evolution [36]. Gold deposition can be achieved by simple immersion of the Pd@PIM-EA-TB modified Nylon disks into a solution of 5 mM KAuCl_4 in 10 mM phosphate buffer at pH 7 for 20 h. Figure 5 shows SEM images and EDX analysis demonstrating the growth of gold in regions where palladium is present as nucleation site (to nucleate gold) and as water oxidation site (to drive gold deposition).

The presence of gold is confirmed in TEM images. Figure 6 shows typical regions with gold dominating over palladium. Figure 7 shows images where both gold and palladium nanoparticles can be seen side-by-side. Gold deposits are observed with typically 10- to 35-nm diameter, often inter-grown into bigger aggregates. Visible also are some remaining palladium nanoparticles without gold modification (see Fig. 7A, B) which may affect the overall reactivity in catalytic processes (*vide infra*).

Clark Probe Measurements

The formation of hydrogen and the consumption of oxygen is conveniently monitored at a commercial Clark probe (Hanna Instruments Ltd.). The Nylon disk (8-mm diameter) was placed onto the Teflon membrane of the probe and fixed into place with an additional Nylon strip. Experiments with PIM-EA-TB directly coated onto the Teflon membrane were unsuccessful probably due to better diffusion through the open

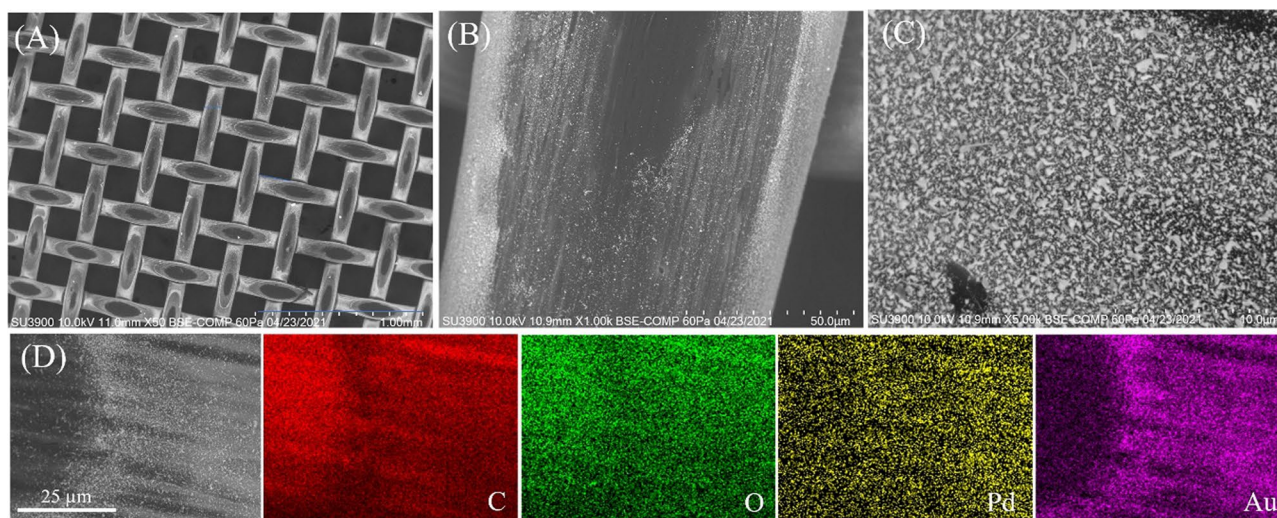


Fig. 5 SEM images with different magnifications **A–C** and EDX elemental mapping analysis **D** for Pd/Au@PIM-EA-TB coated nylon mesh

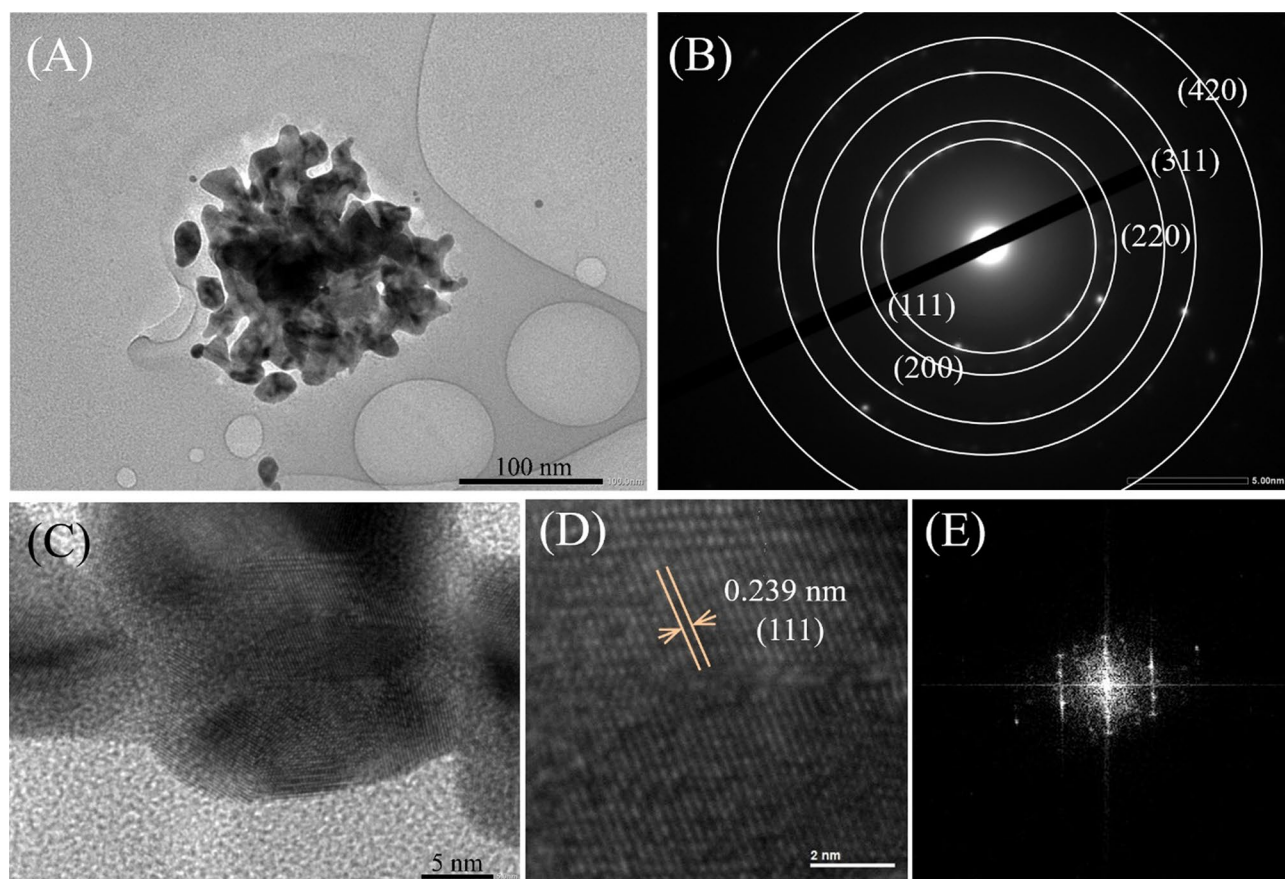


Fig. 6 TEM images for Pd/Au@PIM-EA-TB. **A** Au particles separated by ultrasonication. **B** Selected area electron diffraction (SAED) pattern with Au indexing. **C** Higher magnification of Au particles.

D High-resolution image showing d-spacing of 0.239 nm indexed to (111) facet of Au. **E** Fast Fourier transform (FFT) diffraction patterns from **D**

Nylon mesh (vide infra). Nylon mesh disks provide a convenient and reproducible method to explore/compare catalyst performance. Once immersed into solution, the Clark probe

with Nylon disk can detect oxygen transport from the solution into the sensor or hydrogen flux from the catalyst into the sensor (monitored at different applied potentials). The

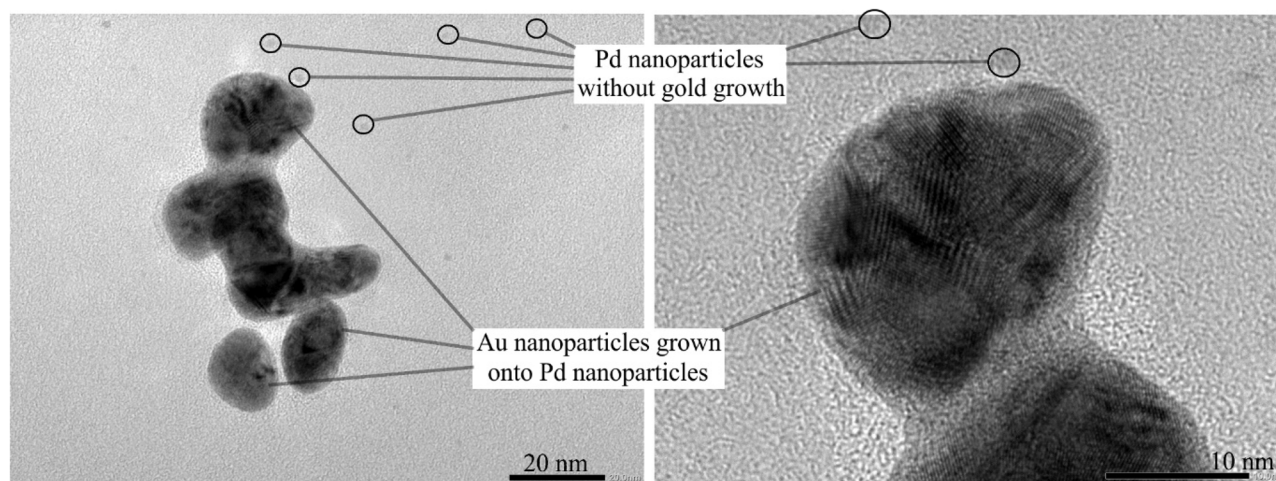
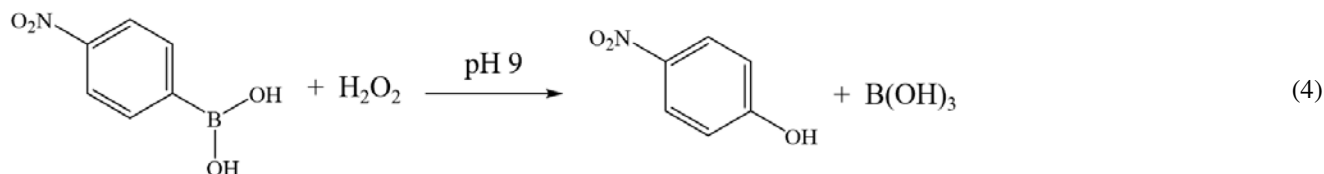


Fig. 7 TEM images for Pd/Au@PIM-EA-TB: bigger Au particles (with size of 10 to 35 nm intergrown into bigger aggregates) attached to small Pd nanoparticles (size of approx. 3.2 nm)

oxygen detection was performed at -0.7 V vs. Ag/AgCl, and the hydrogen production was measured at $+0.6$ V vs. Ag/AgCl [32, 37].

Quantification Measurement of H_2O_2 by LC–MS

The concentration of H_2O_2 produced by catalysts was evaluated indirectly based on the reaction of *para*-nitrophenylboronic acid with H_2O_2 in alkaline conditions [38]. This reaction is often employed in a colorimetric assay, but here, a more powerful LC–MS analysis approach is chosen. The mechanism for formation of the *para*-nitrophenol product is illustrated below (Eq. 4).



The product *para*-nitrophenol is quantified by LC–MS analysis. To generate the standard calibration curve for a range of H_2O_2 concentrations, a volume of $100 \mu\text{L}$ H_2O_2 solution ranging from 2 to $500 \mu\text{M}$ was mixed with 1 mL of $100 \mu\text{M}$ *para*-nitrophenylboronic acid in 10 mM carbonate buffer solution ($\text{pH } 9$ with 10% DMSO), kept in the dark for 1 h , diluted to $1/50$ of the concentration with 10% DMSO/ 90% of water, and then submitted to the LC–MS analysis. For the H_2O_2 quantification in samples, the solution alkalinity was always pre-adjusted to $\text{pH } 9$ by adding Na_2CO_3 powder before commencing the analysis procedure. Mass spectrometry (LC–MS) analyses were performed on an Automated Agilent QTOF (Walkup) used with HPLC (4 chromatography columns) and variable wavelength detector (Agilent QTOF 6545 with Jetstream ESI spray source coupled to an Agilent 1260 Infinity II Quat pump HPLC with 1260 autosampler, column oven compartment, and variable wavelength detector).

Results and Discussion

Clark Probe Evidence for Oxygen Consumption and Hydrogen Production from Formic Acid at Pd@PIM-EA-TB

A Clark probe was employed with Pd@PIM-EA-TB catalyst immobilised on a Nylon mesh substrate (8-mm -diameter disks, see “Experimental”). With the Nylon substrate attached, the Clark probe allows both detection of oxygen consumption (lowering the flux of oxygen into the Clark probe) and detection of hydrogen production (inducing the flux of hydrogen

into the Clark probe). Figure 8 shows typical current–time transient data plots. Figure 8A shows the effect of formic acid on the oxygen detection. Without addition of formic acid, the Clark probe (at -0.7 V vs. Ag/AgCl) equilibrates to about $-0.35 \mu\text{A}$ after 5 min . This corresponds to the oxygen flux from solution through the Nylon disk, through the sensor film, and to the underlying platinum sensor electrode consistent with previous reports [33]. The equilibration time (the time to quasi steady state) of 2 to 5 min is typical, although slower equilibration may be anticipated in the case of additional catalytic reactions at the coated Nylon disk. When adding formic acid, the oxygen signal is clearly lowered. A plot of the oxygen response versus formic acid concentration (Fig. 8B) suggests

that approximately half of the oxygen flux is lost for 2 mM formic acid. For approximately 4 mM formic acid close to all oxygen seems to be consumed locally at the catalyst.

When exploring the production of hydrogen (Fig. 8C) as a function of formic acid, a “switch-on” transition occurs at approximately 10 mM formic acid with more formic acid leading to a plateau in the response probably linked to saturation of the solution with hydrogen. The Clark probe current (with $+0.6$ V vs. Ag/AgCl applied voltage) for high formic acid concentrations is consistent with the response expected when intentionally bubbling hydrogen gas to saturate the solution [33]. When purging the solution with argon gas and then adding formic acid, very similar Clark probe responses are recorded (see Fig. 8D) consistent with the observation that most oxygen is consumed by chemical reaction with 2 mM or more formic acid.

Additional experiments with only Nylon gave no evidence of any background catalytic activity. Experiments with palladium-modified Nylon (employing the same methods but not applying PIM-EA-TB) resulted in some Pd deposit but insignificantly low activity. This suggests that the microporous PIM-EA-TB coating is crucial in (i) initially binding the PdCl_4^{2-} and (ii) for allowing Pd nanoparticles to form embedded into the microporous PIM-EA-TB host as catalytic guests. The microporosity/microenvironment of PIM-EA-TB may have additional effects on reactant and product transport. Fundamentally, net processes at the palladium catalyst can be tentatively suggested based on (Fig. 8A) oxygen consumption (processes 1 and 2, see Eqs. 1 and 2) and (Fig. 8B) based on hydrogen production (process 3, see Eq. 3, Fig. 8E).

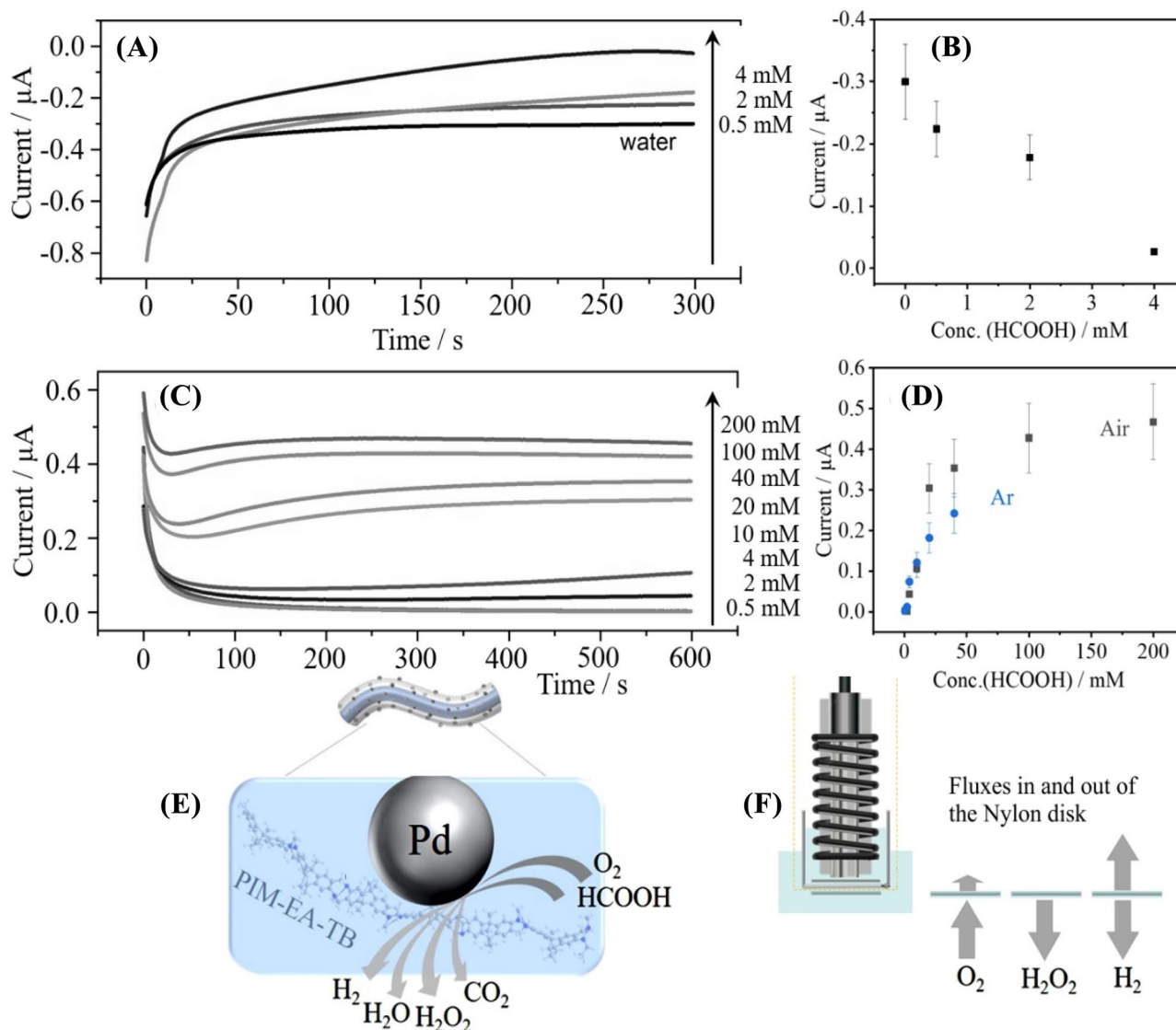


Fig. 8 **A** Clark probe oxygen current–time transients (-0.7 V vs. Ag/AgCl applied voltage) in water, 0.5 mM, 2 mM, and 4 mM formic acid. **B** Plot of the approximate Clark probe oxygen responses versus formic acid concentration. **C** Clark probe hydrogen current–time transients ($+0.6$ V vs. Ag/AgCl applied voltage) in 0.5 to 200 mM formic

acid. **D** Plot of the approximate Clark probe hydrogen response versus formic acid concentration (error bars estimated $\pm 20\%$). **E** Schematic illustration of catalytic reactions at Pd. **F** Illustration of fluxes to and from the Nylon disk with catalyst

In order to discuss processes at the catalyst, it is helpful to consider fluxes to/from the Nylon disk (see Fig. 8F). The corresponding flux of oxygen into the Clark probe can be dissected and compared to the diffusion of oxygen from bulk solution and reactive flux at the catalyst. For the reactive flux density of process 1 (in $\text{mol m}^{-2} \text{s}^{-1}$), an expression rate (process 1) $= \Phi_{\text{Process 1}} = k_1 [\text{HCOOH}] [\text{O}_2]$ can be suggested with formally k_1 (in $\text{mol}^{-1} \text{m}^4 \text{s}^{-1}$) representing the apparent rate constant for the surface catalytic processes within the

PIM-EA-TB on the Nylon substrate. The oxygen flux density (based on the same units $\text{mol m}^{-2} \text{s}^{-1}$), $\Phi_{\text{oxygen transport}}$, in quiescent solution can be estimated as $\Phi_{\text{oxygen transport}} = D_{\text{oxygen}} [\text{O}_2] / \delta$ with the approximate diffusion coefficient for oxygen $D_{\text{oxygen}} = 3 \times 10^{-9} \text{m}^2 \text{s}^{-1}$ [39], the bulk concentration of oxygen typically $[\text{O}_2] = 0.2 \text{mol m}^{-3}$ [39], and the diffusion layer thickness due to natural convection in aqueous media estimated as approximately $\delta = 0.5 \text{mm}$. The resulting flux density for oxygen is $\Phi_{\text{oxygen transport}} = 1.2 \times 10^{-6} \text{mol m}^{-2} \text{s}^{-1}$. The case

of equal flux densities (that is, oxygen is consumed without entering the Clark probe) was observed for $[\text{HCOOH}] = 4 \text{ mM}$, which allows the apparent rate constant for process 1 to be estimated from $\Phi_{\text{oxygen transport}} \approx \Phi_{\text{Process 1}} = k_1 [\text{HCOOH}] [\text{O}_2]$ as $k_1 = 1.5 \times 10^{-6} \text{ mol}^{-1} \text{ m}^4 \text{ s}^{-1}$. This rate constant describes the consumption of oxygen under these conditions (for a given Galvani potential, *vide infra*) and will be discussed in more detail below.

For the production of hydrogen, the concentration at which hydrogen saturation in solution occurs at about $[\text{HCOOH}] = 100 \text{ mol m}^{-3}$ (see Fig. 8C) can be employed to further explore reaction rates. The rate for process 3 formally is rate (process 3) = $k_3 [\text{HCOOH}]$ with k_3 being estimated at the point of saturation linked to the insufficient diffusion of hydrogen away from the Clark probe. The flux density for hydrogen is $\Phi_{\text{hydrogen transport}} = D_{\text{hydrogen}} [\text{H}_2] / \delta$ with $D_{\text{hydrogen}} = 9 \times 10^{-9} \text{ m}^2 \text{ s}^{-1}$ [40] and $[\text{H}_2]$ representing the saturation concentration 0.74 mol m^{-3} . Combining the flux density for hydrogen and the formal rate equation for process 3, rate (process 3) = $\Phi_{\text{Process 3}} = k_3 [\text{HCOOH}]$, gives an estimate of the apparent rate constant $k_3 = 1.3 \times 10^{-7} \text{ m s}^{-1}$ (under the conditions of this experiment). For $[\text{O}_2] = 0.2 \text{ mM}$, the flux densities $\Phi_{\text{Process 1}}$ and $\Phi_{\text{Process 3}}$ are very similar (assuming that processes 2 and 4 are valid). In order to explore/compare, the rate for process 2 methods for H_2O_2 detection/monitoring needs to be applied (*vide infra*).

When performing experiments and monitoring the evolution of hydrogen at formic acid concentration higher than 0.2 M, some deterioration of the catalyst performance can be observed upon going back to lower concentrations (not shown). There have been previous reports of palladium catalyst deterioration at higher formic acid concentrations being linked catalyst poisoning [41], but no clear mechanism has been assigned.

Clark Probe Evidence for Oxygen Consumption and Hydrogen Evolution from Formic Acid at Pd/Au@PIM-EA-TB

When electrolessly coating the palladium catalyst with gold (see experimental), a new pattern of reactivity emerges. The modified palladium is likely to interact with formic acid in a similar manner to give CO_2 , protons, and electrons, but the electrons are now allowed to flow into the gold (with substantially higher surface area; see illustration in Fig. 9). Gold is known to produce hydrogen peroxide during oxygen reduction under mild conditions [42]. The Pd/Au assembly acts as bipolar catalyst.

Figure 9A shows typical Clark probe responses (at -0.7 V vs. Ag/AgCl) for oxygen removal in the presence of formic acid. The plot in Fig. 9B shows that at about 20 mM formic acid half of the oxygen is consumed. Complete consumption of oxygen occurs at approximately 40 mM formic acid. Formally,

this suggests a process 1 rate constant k_1 an order of magnitude lower ($k_1 \approx 1.5 \times 10^{-7} \text{ mol}^{-1} \text{ m}^4 \text{ s}^{-1}$) compared to that estimated for Pd@PIM-EA-TB (see Fig. 8). The main reasons for this drop in reactivity towards oxygen consumption are the lower availability of catalytic palladium surface (although some individual palladium nanoparticles are still observed in the TEM data in Fig. 7) and a less negative Galvani potential developing on palladium/gold nanoparticle assemblies (*vide infra*)

Similarly, the production of hydrogen seems severely suppressed. Figure 9C shows data for hydrogen production at different formic acid concentrations. Hydrogen is clearly detected, but even with a high concentration of 1 M formic acid, the rate of hydrogen production remains low (possibly kinetically rather than transport limited). This is consistent with significant deactivation towards hydrogen production of the palladium in Pd/Au@PIM-EA-TB. Overall, the catalyst in the presence of gold seems severely deactivated in terms of hydrogen production to approximately 1% of the activity observed without gold. In contrast, the production of hydrogen peroxide as a key intermediate in the reduction of oxygen (see process 1) could be enhanced under these conditions. Therefore, the production of H_2O_2 is considered next.

Evidence for Hydrogen Peroxide Formation from Oxygen and Formic Acid

In order to detect hydrogen peroxide, H_2O_2 , as a product of the catalytic reaction (process 1), a method based on the reaction of *para*-nitrophenyl-boronic acid to *para*-nitrophenol was developed (see experimental), and the *para*-nitrophenol detection was performed with HPLC–MS to give a calibration range from 2 to 500 μM H_2O_2 . Here, the bulk concentration of H_2O_2 is probed, and from this, the flux towards the Nylon disk is estimated. Experiments are performed in a stirred solution, and therefore, the rate of mass transport towards the catalyst is likely to be approximately 20 times higher compared to quiescent conditions at the Clark probe (assuming an order of magnitude increase in mass transport and access to both sides).

Figure 10A shows how hydrogen peroxide is produced with time. In the presence of 2 mM formic acid and ambient oxygen levels (approx. 0.2 mM [39]), a gradual increase (approximately linear) is observed leading to approx. 20 μM H_2O_2 after 2 h of reaction (for one Pd@PIM-EA-TB modified 8-mm diameter Nylon disk in a volume of 10 cm^3 stirred solution). This is consistent with gradual transport of H_2O_2 from the Nylon disk into the bulk solution. Figure 10B shows data obtained at 2 h reaction time as a function of formic acid concentration (note that volume is 2 cm^3). The point of the highest rate of H_2O_2 production with 2 mM formic acid corresponds to a H_2O_2 flux density of

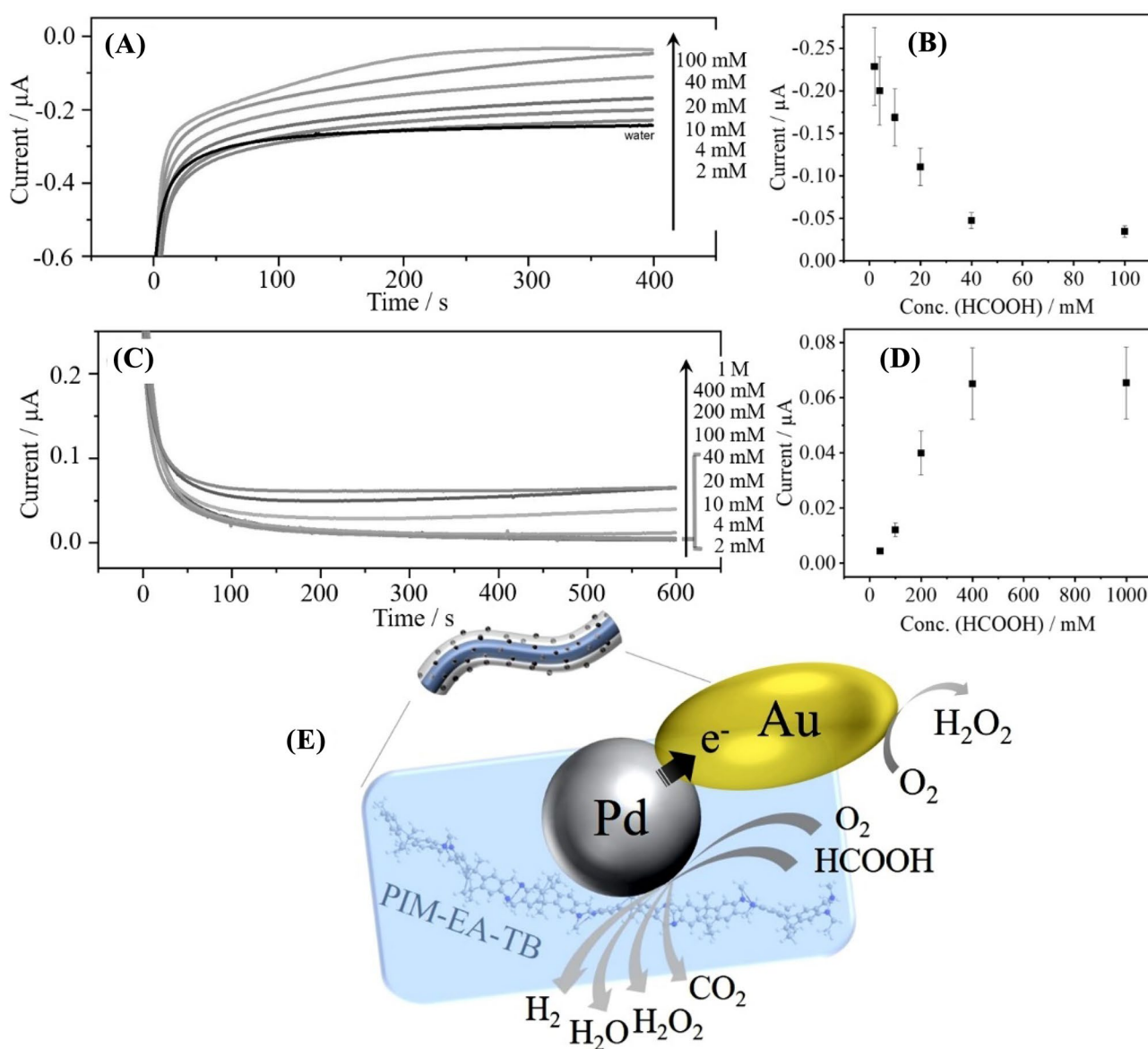


Fig. 9 **A** Clark probe oxygen current time transients in water, 2 mM, 4 mM, 10 mM, 20 mM, 40 mM, and (vii) 100 mM formic acid. **B** Plot of the approximate Clark probe oxygen response versus formic acid concentration (error bars estimated $\pm 20\%$). **C** Clark probe hydro-

gen current time transients in 2 to 1000 mM formic acid. **D** Plot of the approximate Clark probe hydrogen response versus formic acid concentration (error bars estimated $\pm 20\%$). **E** Schematic illustration (not to scale) of catalytic reactions at Pd/Au

$\Phi_{\text{Process 1}} = 1.1 \times 10^{-7} \text{ mol m}^{-2} \text{ s}^{-1}$, which is very low when compared to the anticipated/estimated oxygen flux density of $\Phi_{\text{oxygen transport}} = 2.4 \times 10^{-5} \text{ mol m}^{-2} \text{ s}^{-1}$ under these conditions (assumed 20 times higher compared to the flux to the Clark probe, vide supra). The reaction progress must be strongly affected by loss/degradation of H_2O_2 according to process 2.

In Fig. 10B, beyond the maximum in H_2O_2 production at 2 mM formic acid the yield of H_2O_2 decreases again. This can be explained based on the ability of Pd nanoparticles to reduce H_2O_2 to H_2O . The data are consistent with sufficient flux of oxygen towards the Nylon disk, where locally (in the

PIM-EA-TB), the increase in the formic acid concentration from 2 to 4 mM causes more reduction of H_2O_2 to H_2O (vide supra).

Figure 10C shows data for the production of H_2O_2 with time for Pd/Au@PIM-EA-TB catalyst. In this case, 10 mM formic acid was employed to drive the process. When compared to data in Fig. 10A, the rate of H_2O_2 production seems approximately 5-times higher consistent with the 5-times higher concentration of formic acid. Figure 10D shows the H_2O_2 yield at 2-h reaction time as a function of formic acid concentration. In the presence of gold, an order of magnitude increase in H_2O_2 yields is evident. From this, the

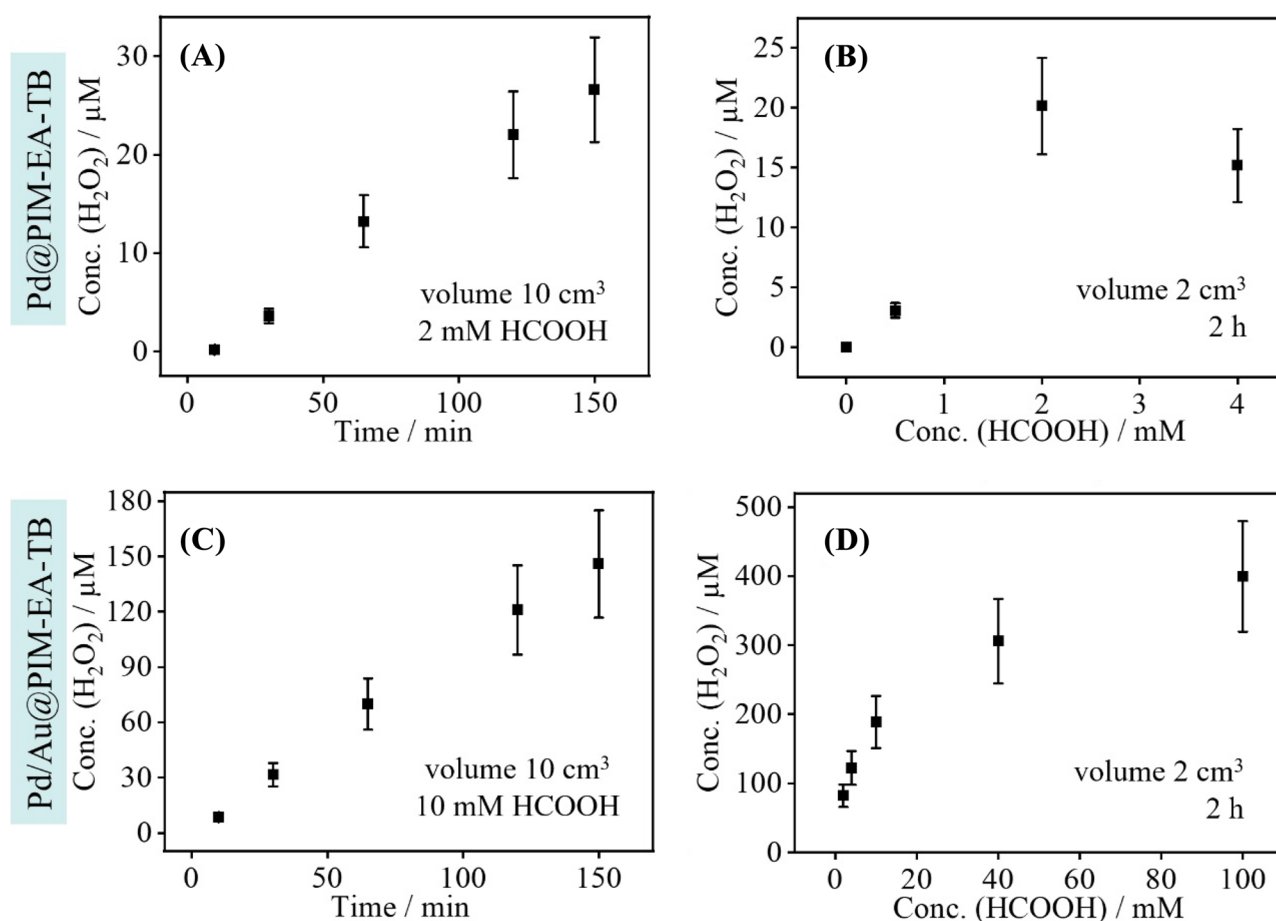


Fig. 10 **A** Plot of H₂O₂ concentration as a function of time (one Nylon disk modified with Pd@PIM-EA-TB in 10 mL stirred solution) for 2 mM formic acid concentration. **B** Plot of H₂O₂ concentration after 120-min reaction (one nylon disk modified with Pd@PIM-EA-TB in 2 mL stirred solution) as a function of formic acid concentration. **C** Plot of H₂O₂ concentration as a function of time (one Nylon

disk modified with Pd/Au@PIM-EA-TB in 10 mL stirred solution) for 10 mM formic acid concentration. **D** Plot of H₂O₂ concentration after 120-min reaction (one Nylon disk modified with Pd/Au@PIM-EA-TB in 2 mL stirred solution) as a function of formic acid concentration (error bars based on variations in catalyst disks and Clark probe responses estimated $\pm 20\%$)

approximate H₂O₂ flux density at the Nylon disk can be calculated as $\Phi_{\text{Process 1}} = 1.0 \times 10^{-7} \text{ mol m}^{-2} \text{ s}^{-1}$ in the presence of 10 mM formic acid. The production of H₂O₂ further increases with formic acid concentration (see Fig. 10D) and, finally, plateaus at high formic acid concentration with $\Phi_{\text{Process 1}} = 2.2 \times 10^{-7} \text{ mol m}^{-2} \text{ s}^{-1}$. This value is still low when compared to the anticipated oxygen flux, and therefore, oxygen transport is unlikely to significantly affect the production of H₂O₂. Under conditions of high formic acid concentration, a plateau suggests that a steady state is approached and that the process becomes independent of [HCOOH]. Combining the rate expressions for process 1 and process 2 (Eqs. 2 and 3) for the case of high [HCOOH] suggests that $k_1/k_2 = [\text{H}_2\text{O}_2]/[\text{O}_2]$. With $k_1 = 1.5 \times 10^{-6} \text{ mol}^{-1} \text{ m}^4 \text{ s}^{-1}$ and $[\text{H}_2\text{O}_2] = 0.4 \text{ mM}$ and $[\text{O}_2] = 0.2 \text{ mM}$, this gives an apparent rate constant $k_2 = \frac{1}{2} k_1 = 0.75 \times 10^{-7} \text{ mol}^{-1} \text{ m}^4 \text{ s}^{-1}$ for the case of Pd/Au@PIM-EA-TB. Although

the production of H₂O₂ is significant, it could be further improved for example based on the oxygen available in solution

It is interesting to further explore the reactivity of Pd/Au@PIM-EA-TB for the production of hydrogen peroxide. Figure 11A shows data for the effect of doubling the amount of catalyst (using one Nylon disk and using two Nylon disks in a stirred solution). Perhaps surprisingly, only at short times (for low [H₂O₂]), the production of H₂O₂ is enhanced. For 1 h or longer reaction times, the effect of increasing the amount of catalyst seems insignificant. A change in the amount of catalyst will affect the apparent rate constants k_1 and k_2 , but not the long-term steady state concentration of H₂O₂ that is given by the ratio of k_1/k_2 . That is, for longer periods of reaction or for higher formic acid concentrations, the same limiting concentration $[\text{H}_2\text{O}_2]_{\text{lim}}$ is generated independently of the amount of catalyst.

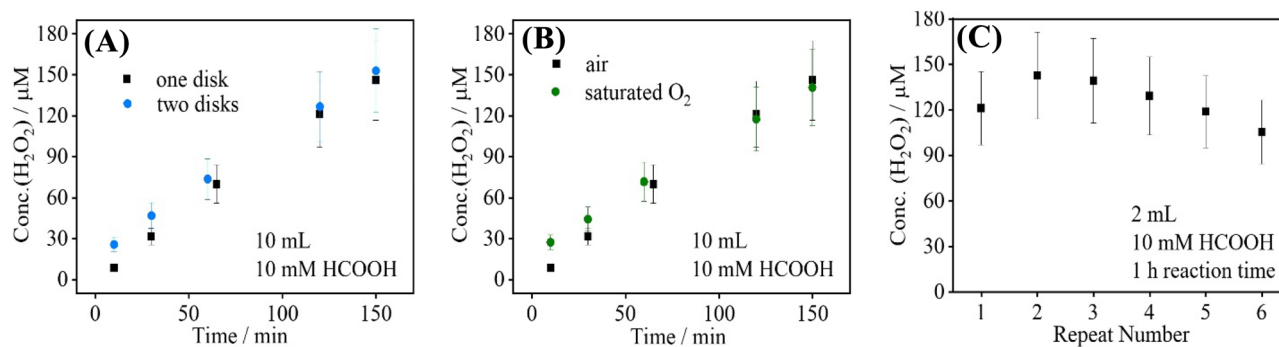


Fig. 11 **A** Plot of H₂O₂ concentration formed at Pd/Au@PIM-EA-TB in the presence of 10 mM formic acid as a function of time. Data sets for (i) one Nylon disk and (ii) two Nylon disks modified with Pd/Au@PIM-EA-TB in 10 cm³ stirred solution. **B** Plot of H₂O₂ concentration formed at Pd/Au@PIM-EA-TB in the presence of 10 mM formic acid as a function of time. Data sets for (i) 0.2 mM oxygen and (ii) 1 mM oxygen for one Nylon disk modified with Pd/Au@

PIM-EA-TB in 10 cm³ stirred solution. **C** Plot of H₂O₂ concentration formed at Pd/Au@PIM-EA-TB in the presence of 10 mM formic acid at 1 h reaction time for repeat experiments (one Nylon disk modified with Pd/Au@PIM-EA-TB in 2 cm³ stirred solution) (error bars based on variations in catalyst disks and Clark probe responses estimated ± 20%)

Figure 11B demonstrates the effect of changing the concentration of oxygen from ambient (approx. 0.2 mM) to saturated (approx. 1.0 mM). The data suggest a significant increase in H₂O₂ production only during the initial 30 min, and a value converging with time. The final value [H₂O₂]_{lim} obtained in the presence of saturated [O₂] could be increased, but the data recorded over a period of 150 min suggests a very similar trend. Finally, Fig. 11C shows that the re-use of the catalyst-modified Nylon disks is possible. For 10 mM formic acid, the production of hydrogen peroxide remains approximately constant in 6 sequential experiments producing H₂O₂ each over a period of 1 h

The catalytic production of H₂O₂ on a bipolar Pd/Au nanocatalyst can be discussed in terms of individual redox processes and assuming Tafel law effects on kinetics linked to the Galvani potential of the catalyst particles. That is, apparent rate constants observed under specific reaction conditions are variable with potential similar to heterogeneous charge transfer rate constants. The scheme in Fig. 12A illustrates the case of formic acid spontaneously producing hydrogen and then hydrogen being oxidised to protons. The rate for this process is Galvani potential dependent (assumed here to follow Tafel characteristics) and indicated as a line. The oxidation is faster at higher potentials. Also indicated is the line for the reduction

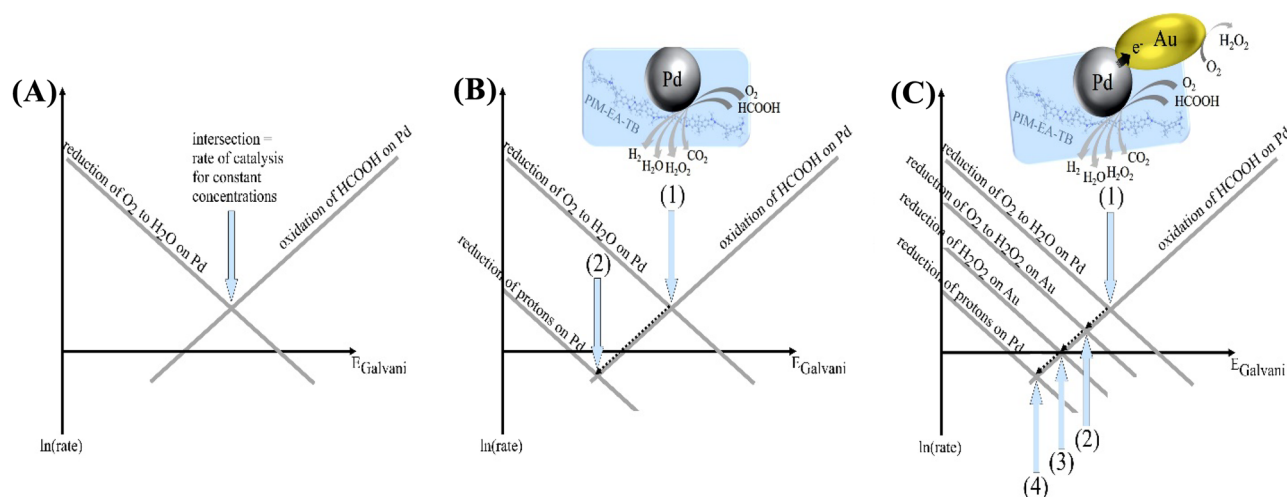


Fig. 12 Schematic illustration of the effect of the Galvani potential on the reaction rate. **A** Oxidation of formic acid and reduction of oxygen leads to a mixed potential on Pd. **B** On Pd oxidation of formic acid and reduction of oxygen form mixed potential (1) and after depletion

of oxygen the potential shifts to (2). **C** On Pd/Au oxidation of formic acid on Pd leads to a mixed potential for reduction of O₂ on Pd (1), then reduction of O₂ to H₂O₂ on Au (2), then reduction of H₂O₂ on Au (3), and, finally, reduction of protons to hydrogen (4)

of oxygen to water. The point of intersection denotes the operational potential during catalysis at a given concentration of reagents. Figure 12B illustrates the effect of oxygen depletion. Due to oxygen being consumed, the rate for the oxygen reduction slows down and the intersection point (1) moves along the line to point (2). Point (2) corresponds to the equilibrium potential for H^+/H_2 at more negative potentials.

The case for the bipolar Pd/Au catalyst is illustrated in Fig. 12C. Initially, the catalyst operates at potential (1) where oxygen is reduced on Pd mainly to water. Depletion of oxygen then shifts the potential to point (2) where oxygen is reduced to H_2O_2 on Au. This corresponds to the optimum working conditions for the bipolar catalyst with further depletion of oxygen pushing the Galvani potential more negative where H_2O_2 is consumed again (3). For a good conversion of oxygen to H_2O_2 (i), the process at point (1) needs to be suppressed by adjusting the ratio of Pd to Au surface area, (i) the process at point (2) needs to be optimised by providing a high Au surface area, and (iii) the concentration of formic acid has to be selected to maintain the operational potential of the bipolar catalysts close to (2).

The polymer of intrinsic microporosity is likely to affect locally the mass transport of formic acid, oxygen, and hydrogen peroxide and is therefore also likely to affect H_2O_2 yields. Further work is required to explore effects for different types of polymers of intrinsic microporosity on these catalytic processes. The yields for H_2O_2 observed in this study are modest and should be much higher with more optimisation. Recent progress in the catalytic production of H_2O_2 directly from H_2 and O_2 gas at PdAu alloy catalysts suggests that up to 56 mM H_2O_2 in water can be achieved [43]. This is two orders of magnitude higher compared to yields reported here. Clearly, more work will be necessary to compare/improve reactivity, to optimise conditions, and to resolve/exploit PIM host effects in this process in the future.

Conclusions

It has been shown that both nano-Pd and nano-Pd/Au catalysts can be formed embedded inside of the microporous host polymer PIM-EA-TB. In the presence of formic acid, both types of catalyst were shown with a Clark probe to consume oxygen and to produce hydrogen. Pd is effective in producing hydrogen, whereas Pd/Au appears to be ineffective. High concentrations of formic acid can be detrimental and may deactivate the catalysts.

In the formic acid concentration range where oxygen consumption and hydrogen production switch over (as observed with the Clark probe), maximum hydrogen peroxide production rates were observed. In contrast to nano-Pd, bipolar nano-Pd/Au catalysts clearly produce higher levels of hydrogen peroxide with only minimal production

of hydrogen even at high formic acid concentrations. This has been attributed to electron transport from Pd to Au and a less negative Galvani potential on the nano-Pd/Au catalyst during operation. Formic acid reacts on Pd followed by electron transfer to gold. On gold, oxygen is reduced primarily to H_2O_2 .

The role of the intrinsically microporous polymer, PIM-EA-TB, in these catalytic reactions is associated with (i) providing a reaction environment for binding Pd(II) and for producing embedded palladium nanoparticles, (ii) for allowing the growth of gold nanoparticles attached to palladium seeds, (iii) for permeation of reactants and products, and (iv) for making the catalysts recoverable and re-usable. The tertiary amine functional group in PIM-EA-TB is essential for the initial binding of PdCl_4^{2-} but could have additional effects on the catalytic process, for example when binding or permeating reaction intermediates. In the future, the molecular structure of PIM-EA-TB could be modified or tuned to allow better/more selective catalytic processes to be developed. For further optimisation of H_2O_2 production from organic reducing agents such as formic acid, the suppression of H_2O_2 degradation (process 2) appears to be crucial and this could be achieved for example by adjusting the ratio of Pd to Au surface area.

Funding L.W. received a PhD stipend from the China Scholarship Council (201906870022). F.M. received support under project EP/K004956/1 from the EPSRC.

Open Access This article is licensed under a Creative Commons Attribution 4.0 International License, which permits use, sharing, adaptation, distribution and reproduction in any medium or format, as long as you give appropriate credit to the original author(s) and the source, provide a link to the Creative Commons licence, and indicate if changes were made. The images or other third party material in this article are included in the article's Creative Commons licence, unless indicated otherwise in a credit line to the material. If material is not included in the article's Creative Commons licence and your intended use is not permitted by statutory regulation or exceeds the permitted use, you will need to obtain permission directly from the copyright holder. To view a copy of this licence, visit <http://creativecommons.org/licenses/by/4.0/>.

References

1. R. Tao, X.R. Ma, X.L. Wei, Y.H. Jin, L. Qiu, W. Zhang, Porous organic polymer material supported palladium nanoparticles. *J. Mater. Chem. A* **8**(34), 17360–17391 (2020)
2. F.X. Felpin, T. Ayad, S. Mitra, Pd/C: an old catalyst for new applications - its use for the Suzuki-Miyaura reaction. *Europ. J. Org. Chem.* **2006**(12), 2679–2690 (2006)
3. A.R. Bayguzina, R.I. Khusnutdinov, Catalytic N-alkylation of anilines. *Russ. J. Gen. Chem.* **91**(3), 305–347 (2021)

- F. Menegazzo, M. Signoretto, E. Ghedini, G. Strukul, Looking for the “dream catalyst” for hydrogen peroxide production from hydrogen and oxygen. *Catalysis* **9**(3), 251 (2019)
- R. Dittmeyer, J.D. Grunwaldt, A. Pashkova, A review of catalyst performance and novel reaction engineering concepts in direct synthesis of hydrogen peroxide. *Catal. Today* **248**, 149–159 (2015)
- N. Dimitratos, J.A. Lopez-Sanchez, G.J. Hutchings, Green catalysis with alternative feedstocks. *Topics Catalysis* **52**(3), 258–268 (2009)
- M.J. Zhong, Y.S. Xu, J. Li, Z.X. Ge, C.M. Jia, Y. Chen, P.L. Deng, X.L. Tian, Engineering PdAu nanowires for highly efficient direct methane conversion to methanol under mild conditions. *J. Phys. Chem. C* **125**(23), 12713–12720 (2021)
- I. Saldan, Y. Semenyuk, I. Marchuk, O. Reshetnyak, Chemical synthesis and application of palladium nanoparticles. *J. Mater. Sci.* **50**(6), 2337–2354 (2015)
- H. Zhong, M. Iguchi, M. Chatterjee, Y. Himeda, Q. Xu, H. Kawanami, Formic acid-based liquid organic hydrogen carrier system with heterogeneous catalysts. *Adv. Sustain. Systems* **2**(2), 1700161 (2018)
- M.C. Luo, Y. Yang, Y.J. Sun, Y.N. Qin, C.J. Li, Y.J. Li, M.G. Li, S. Zhang, D. Su, S.J. Guo, Ultrathin two-dimensional metallic nanocrystals for renewable energy electrocatalysis. *Mater. Today* **23**, 45–56 (2019)
- S.M.S. Hussain, M.S. Kamal, M.K. Hossain, Recent developments in nanostructured palladium and other metal catalysts for organic transformation. *J. Nanomater.* **2019**, 1562130 (2019)
- K. Halder, G. Bengtson, V. Filiz, V. Abetz, Catalytically active (Pd) nanoparticles supported by electrospun PIM-1: influence of the sorption capacity of the polymer tested in the reduction of some aromatic nitro compounds. *Appl. Catal. A-Gen.* **555**, 178–188 (2018)
- H.R. Moon, D.W. Lim, M.P. Suh, Fabrication of metal nanoparticles in metal-organic frameworks. *Chem. Soc. Rev.* **42**, 1807–1824 (2013)
- Z.X. Low, P.M. Budd, N.B. McKeown, D.A. Patterson, Gas permeation properties, physical aging, and its mitigation in high free volume glassy polymers. *Chem. Rev.* **118**, 5871–5911 (2018)
- N.B. McKeown, P.M. Budd, Polymers of intrinsic microporosity (PIMs): organic materials for membrane separations, heterogeneous catalysis and hydrogen storage. *Chem. Soc. Rev.* **35**, 675–683 (2006)
- L.N. Wang, Y.Z. Zhao, B.B. Fan, M. Carta, R. Malpass-Evans, N.B. McKeown, F. Marken, Polymer of intrinsic microporosity (PIM) films and membranes in electrochemical energy storage and conversion: a mini-review. *Electrochem. Commun.* **118**, 106798 (2020)
- F. Marken, E. Madrid, Y.Z. Zhao, M. Carta, N.B. McKeown, Polymers of intrinsic microporosity in triphasic electrochemistry: perspectives. *ChemElectroChem* **6**, 4332–4342 (2019)
- S.D. Ahn, A. Kolodziej, R. Malpass-Evans, M. Carta, N.B. McKeown, S.D. Bull, A. Buchard, F. Marken, Polymer of intrinsic microporosity induces host-guest substrate selectivity in heterogeneous 4-benzoyloxy-TEMPO-catalysed alcohol oxidations. *Electrocatalysis* **7**, 70–78 (2016)
- Y.Z. Zhao, N.A. Al Abass, R. Malpass-Evans, M. Carta, N.B. McKeown, E. Madrid, P.J. Fletcher, F. Marken, Photoelectrochemistry of immobilised Pt@g-C₃N₄ mediated by hydrogen and enhanced by a polymer of intrinsic microporosity PIM-1. *Electrochem. Commun.* **103**, 1–6 (2019)
- D.P. He, D.S. He, J.L. Yang, Z.X. Low, R. Malpass-Evans, M. Carta, N.B. McKeown, F. Marken, Molecularly rigid microporous polyamine captures and stabilizes conducting platinum nanoparticle networks. *ACS Appl. Mater. Interfaces* **8**, 22425–22430 (2016)
- R.K. Adamik, N. Hernandez-Ibanez, J. Iniesta, J.K. Edwards, A.G.R. Howe, R.D. Armstrong, S.H. Taylor, A. Roldan, Y.Y. Rong, R. Malpass-Evans, M. Carta, N.B. McKeown, D.P. He, F. Marken, Platinum nanoparticle inclusion into a carbonized polymer of intrinsic microporosity: electrochemical characteristics of a catalyst for electroless hydrogen peroxide production. *Nanomaterials* **8**, 542 (2018)
- E. Madrid, Y.Y. Rong, M. Carta, N.B. McKeown, R. Malpass-Evans, G.A. Attard, T.J. Clarke, S.H. Taylor, Y.T. Long, F. Marken, Metastable ionic diodes derived from an amine-based polymer of intrinsic microporosity. *Angew. Chem. Inter. Ed.* **53**, 10751–10754 (2014)
- Y.Y. Rong, A. Kolodziej, E. Madrid, M. Carta, R. Malpass-Evans, N.B. McKeown, F. Marken, Polymers of intrinsic microporosity in electrochemistry: anion uptake and transport effects in thin film electrodes and in free-standing ionic diode membranes. *J. Electroanal. Chem.* **779**, 241–249 (2016)
- Y. Liu, X.K. Zeng, X.Y. Hu, Y. Xia, X.W. Zhang, Solar-driven photocatalytic disinfection over 2D semiconductors: the generation and effects of reactive oxygen species. *Solar RRL* **5**, 2000594 (2021)
- N. Dimitratos, J.A. Lopez-Sanchez, G.J. Hutchings, Green catalysis with alternative feedstocks. *Topics Catal.* **52**, 258–268 (2009)
- P.N.R. Vennestrom, C.H. Christensen, S. Pedersen, J.D. Grunwaldt, J.M. Woodley, Next-generation catalysis for renewables: combining enzymatic with inorganic heterogeneous catalysis for bulk chemical production. *ChemCatChem* **2**, 249–258 (2010)
- J.S. Hu, P.F. Zhang, W.J. An, L. Liu, Y.H. Liang, W.Q. Cui, In-situ Fe-doped g-C₃N₄ heterogeneous catalyst via photocatalysis-Fenton reaction with enriched photocatalytic performance for removal of complex wastewater. *Appl. Catal. B Environm.* **245**, 130–142 (2019)
- B.M. Choudary, M.L. Kantam, P.L. Santhi, New and ecofriendly options for the production of speciality and fine chemicals. *Catal. Today* **57**, 17–32 (2000)
- J.J. Gao, B. Liu, Progress of electrochemical hydrogen peroxide synthesis over single atom catalysts. *ACS Mater. Lett.* **2**, 1008–1024 (2020)
- A. Torres-Pinto, M.J. Sampaio, C.G. Silva, J.L. Faria, A.M.T. Silva, Recent strategies for hydrogen peroxide production by metal-free carbon nitride photocatalysts. *Catalysis* **9**, 990 (2019)
- hydrogen peroxide as intermediate and reagent, M. Comotti, C. Della Pina, E. Falletta, M. Rossi, Aerobic oxidation of glucose with gold catalyst. *Adv. Synth. Catal.* **348**, 313–316 (2006)
- M.S. Yalfani, S. Contreras, F. Medina, J. Sueiras, Direct generation of hydrogen peroxide from formic acid and O₂ using heterogeneous Pd/gamma-Al₂O₃ catalysts. *Chem. Commun.* **3885–3887**, 8 (2008)
- Y.Z. Zhao, R. Malpass-Evans, M. Carta, N.B. McKeown, P.J. Fletcher, G. Kociok-Kohn, D. Lednitzky, F. Marken, Size-selective photoelectrochemical reactions in microporous environments: clark probe investigation of Pt@g-C₃N₄ embedded into intrinsically microporous polymer (PIM-1). *ChemElectroChem* (2021). <https://doi.org/10.1002/celec.202100732>
- M. Carta, R. Malpass-Evans, M. Croad, Y. Rogan, J.C. Jansen, P. Bernardo, F. Bazzarelli, N.B. McKeown, An efficient polymer molecular sieve for membrane gas separations. *Science* **339**, 303–307 (2013)
- F.J. Xia, M. Pan, S.C. Mu, R. Malpass-Evans, M. Carta, N.B. McKeown, G.A. Attard, A. Brew, D.J. Morgan, F. Marken, Polymers of intrinsic microporosity in electrocatalysis: novel pore rigidity effects and lamella palladium growth. *Electrochim. Acta* **128**, 3–9 (2014)
- T. Kanyanee, P.J. Fletcher, E. Madrid, F. Marken, Indirect (hydrogen-driven) electrodeposition of porous silver onto a palladium membrane. *J. Solid State Electrochem.* **24**, 2789–2796 (2020)

37. D. Mislov, M. Cifrek, I. Krois, H. Dzapov, Measurement of dissolved hydrogen concentration with Clark electrode. *IEEE Sens. Appl. Symp.* 504–508 (2015)
38. C.P. Lu, C.T. Lin, C.M. Chang, S.H. Wu, L.C. Lo, Nitrophenylboronic acids as highly chemoselective probes to detect hydrogen peroxide in foods and agricultural products. *J. Agricultural Food Chem.* **59**, 11403–11406 (2011)
39. J. Weber, A.J. Wain, F. Marken, Microwire chronoamperometric determination of concentration, diffusivity, and salinity for simultaneous oxygen and proton reduction. *Electroanalysis* **27**, 1829–1835 (2015)
40. T.E. Crozier, S. Yamamoto, Solubility of hydrogen in water, sea water, and sodium chloride solutions. *J. Chem. Eng. Data* **19**, 242–244 (1974)
41. E. Madrid, C. Harabaiju, R.S. Hill, K. Black, L. Torrente-Murciano, A.J. Dickinson, P.J. Fletcher, K.I. Ozoemena, A.K. Ipadeola, E. Oguzie, C.O. Akalezi, F. Marken, Indirect formic acid fuel cell based on a palladium or palladium-alloy film separating the fuel reaction and electricity generation. *ChemElectroChem* **8**, 378–385 (2021)
42. S. Das, A. Mishra, M.M. Ghangrekar, Production of hydrogen peroxide using various metal-based catalysts in electrochemical and bioelectrochemical systems: mini review. *J. Hazardous Toxic Radioactive Waste* **24**, 06020001 (2020)
43. A. Akram, G. Shaw, R.J. Lewis, M. Piccinini, D.J. Morgan, T.E. Davies, S.J. Freakley, J.K. Edwards, J.A. Moulijn, G.J. Hutchings, The direct synthesis of hydrogen peroxide using a combination of a hydrophobic solvent and water. *Catal. Sci. Technol.* **10**, 8203–8212 (2020)

Publisher's Note Springer Nature remains neutral with regard to jurisdictional claims in published maps and institutional affiliations.